J. Fluid Mech. (2005), *vol.* 530, *pp.* 81–100. © 2005 Cambridge University Press
doi:10.1017/S0022112005003514 Printed in the United Kingdom

Study of trajectories of jets in crossflow using direct numerical simulations

By SUMAN MUPPIDI AND KRISHNAN MAHESH
Aerospace Engineering and Mechanics, University of Minnesota, Minneapolis, MN 55455, USA

(Received 27 April 2004 and in revised form 29 November 2004)

This paper studies the trajectories and near field of round jets in crossflow. Incompressible direct numerical simulations are performed at velocity ratios of 1.5 and 5.7 and the effects of jet velocity profile and boundary layer thickness on the jet trajectory are examined. The 'rd' scaling used at present (Margason 1993) does not contain any information on these parameters, and trajectories scaled by rd do not collapse. The trajectory is strongly influenced by the near field which depends on both the jet velocity profile and the crossflow boundary layer. A length scale is proposed to describe the near field of the jet. An analytical expression is proposed for this length scale which is a measure of the relative inertia of the jet and the crossflow. Incorporating this length scale significantly improves the scaling of the trajectories.

1. Introduction

Jets in crossflow find practical application in many engineering problems like film cooling in turbine blades, pollutant dispersal, fuel injection and dilution holes in combustors. The flow field of a jet in crossflow is believed to be influenced primarily by the effective velocity ratio

$$r = \left\{ \frac{\rho_j u_j^2}{\rho_{cf} u_{cf}^2} \right\}^{1/2}, \tag{1.1}$$

which simplifies to $r = u_j/u_{cf}$ for constant-density flows. Here, u_j is the jet velocity, u_{cf} is the velocity of the crossflow, ρ_j is the density of the jet fluid and ρ_{cf} is the crossflow fluid density.

Margason (1993) provides an extensive review of past work on jets in crossflow. The different vortical features of this flow are described in detail by Fric & Roshko (1994). The counter-rotating vortex pair, considered a predominant feature, has been examined in detail by a number of researchers. Detailed measurements of velocity and vorticity fields in the cross-section of a counter-rotating vortex pair have been performed (Kamotani & Greber 1972; Fearn & Weston 1974) along with measurements of velocity in the symmetry plane (Kelso, Lim & Perry 1996; Andreopoulos & Rodi 1985). Horseshoe vortices (Krothapalli, Lourenco & Buchlin 1990; Kelso & Smits 1995) and the structure of the wake region (Fric & Roshko 1994) have also been studied. Measurements of scalar mixing in jets in crossflow have recently been performed (Smith & Mungal 1998; Su *et al.* 2000; Shan & Dimotakis 2001; Hasselbrink & Mungal 2001*b*) and large-eddy simulations have been used to study coherent structures (Yuan, Sheet & Ferziger 1999) and scalar mixing (Yuan & Street 1998; Schluter & Schonfeld 2000).

https://doi.org/10.1017/S0022112005003514 Published online by Cambridge University Press

The mean jet trajectory is of fundamental interest and has been studied by various investigators. Analytical models to estimate the jet trajectory have been suggested by Broadwell & Breidenthal (1984), Karagozian (1986) and Hasselbrink & Mungal (2001*a*). Karagozian considers a vortex pair issuing from the jet orifice and into the crossflow. Numerical solution of the equations governing the evolution of this vortex pair gives the power law

$$\frac{y}{d} = \alpha r^{\beta} \left(\frac{x}{d}\right)^{\gamma} \tag{1.2}$$

for the trajectory, where d is the diameter of the jet orifice. The constants are $\alpha = 0.527$, $\beta = 1.178$ and $\gamma = 0.314$. Broadwell & Breidenthal (1984) use a similarity theory to treat the jet exit as a point source of momentum. They conclude that the global length scale in the flow is rd in the region away from the jet exit. This length scale is used to scale the trajectory as

$$\frac{y}{rd} = A \left(\frac{x}{rd}\right)^{B} \tag{1.3}$$

where A and B are constants. Pratte & Baines (1967) obtain $A = 2.05$ and $B = 0.28$ using their experimental data. Margason (1993) provides a list of experimental values for A and B. Experimental results show $1.2 < A < 2.6$ and $0.28 < B < 0.34$. Keffer & Baines (1963) find that the trajectories collapse on normalizing the axes with $r^2 d$. However, their data pertained to a region very close to the jet exit (maximum downstream distance of $4d$). Smith & Mungal (1998) perform experiments at velocity ratios ranging from 5 to 25 and find that the trajectories scale most satisfactorily with rd (as compared to scaling with d or $r^2 d$). Hasselbrink & Mungal (2001*a*) employ similarity analysis, similar to that of Broadwell & Breidenthal, and intermediate asymptotics theory to arrive at scaling laws for velocity, mass flux and jet trajectory. They scale the trajectory as

$$\frac{y}{rd} = \left\{\frac{2}{c_{ej}} \frac{x}{rd}\right\}^{1/2} \quad \text{and} \quad \frac{y}{rd} = \left\{\frac{3}{c_{ew}} \frac{x}{rd}\right\}^{1/3} \tag{1.4}$$

in the near field and the far field (wake-like region) respectively. Here, c_{ej} and c_{ew} are the entrainment coefficients in the jet region and the wake-like region respectively.

Figure 1 shows jet trajectories scaled with rd using data from different experiments. Note that the trajectories do not collapse. Considerable difference in the scaled trajectories is seen even for velocity ratios that are fairly close ($r = 5.7$ and 5.81) to each other. Note that Smith & Mungal (1998) and Su *et al.* (2000) define the jet trajectory as the locus of maximum scalar concentration, while the experimental results presented in Kamotani & Greber (1972) and Chochua *et al.* (2000) define jet trajectory as the locus of maximum velocity. It has been noted (Smith & Mungal 1998) that the trajectory based on maximum local velocity penetrates 5–10% deeper into the flow than the trajectory based on maximum scalar concentration. However, the scatter observed in figure 1 far exceeds 5–10% suggesting that its origin is not due to the difference in the definition of jet trajectory. The difference in trajectory between Su *et al.*'s (2000, pipe flow profile jet) and Smith & Mungal's (1998, top-hat profile jet) experiments is reflected in the scalar decay rates (Su *et al.* 2000).

This paper uses direct numerical simulation (DNS) to examine possible reasons for the lack of collapse with rd. The objective is to study the effect of the jet velocity profile and the crossflow boundary layer thickness on the trajectory. DNS of an incompressible round jet in crossflow at two velocity ratios of 1.52 and 5.7

https://doi.org/10.1017/S0022112005003514 Published online by Cambridge University Press

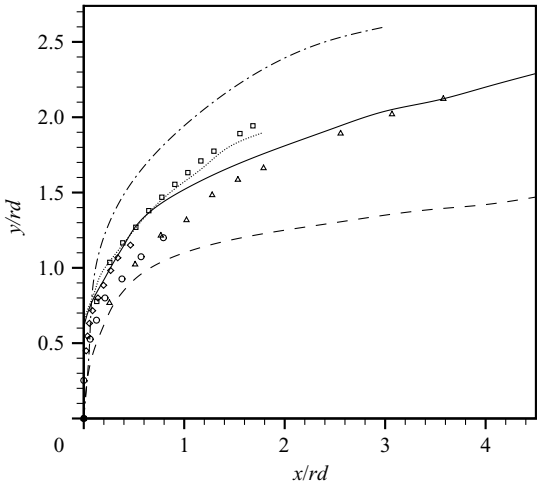


FIGURE 1. Jet trajectories from different experiments scaled by rd: ○, $r = 4.0$ (Keffer & Baines 1963); ◇, $r = 6.0$ (Keffer & Baines 1963); △, $r = 3.9$ (Kamotani & Greber 1972); □, $r = 7.7$ (Kamotani & Greber 1972); ——, $r = 10$ (Smith & Mungal 1998); – – – –, $r = 5$ (Smith & Mungal 1998); ·····, $r = 5.81$ (Chochua *et al.* 2000); —·—, $r = 5.7$ (Su & Mungal 2000).

are performed. By varying the jet velocity profile and the crossflow boundary layer thickness, the dependence of trajectory on these parameters is studied. This paper is organized as follows. Section 2 discusses the problem and details of the simulations. Qualitative flow features observed in the simulations are presented in § 3.1. Section 3.2 presents the jet trajectories and the observed dependence of trajectories on the crossflow boundary layer thickness and the jet velocity profile. The near field of the jet exit is examined in § 3.3. The jet trajectory depends on the near field and a new scaling is proposed in § 4 in terms of the jet near field. The paper ends with a short summary in § 5.

2. Simulation details

2.1. *Problem statement*

Figure 2 shows a schematic of the problem, where a laminar jet issues perpendicularly from a round pipe into a laminar crossflow. The crossflow is in the x-direction and the jet is in the y-direction. The origin is located at the centre of the jet exit as shown. The jet velocity (u_j) is a function of the radial distance from the pipe centre and the crossflow velocity (u_{cf}) varies with distance from the wall. u_∞ is the crossflow free-stream velocity. The velocity ratio is defined as $r = \overline{u}_j/u_\infty$, where $\overline{u_j}$ is the mean jet velocity obtained by averaging u_j over the pipe cross-section.

The simulations are performed at two velocity ratios: $r = 1.52$ and $r = 5.7$, which are representative velocity ratios observed in film cooling and in dilution holes of gas-turbine combustors respectively. The Reynolds number of the flow based on the bulk jet velocity and the pipe diameter is 1500 at $r = 1.52$ and 5000 at $r = 5.7$. Two different velocity profiles for the jet are considered, and are shown in figure 3(*a*). One of them is parabolic and the other has a mean-turbulent profile. Note that given a long enough pipe, it may be expected that the mean-turbulent profile changes to a laminar profile. However, this transition is due to the viscous stresses. The Reynolds numbers in the present simulations are high enough that the mean-turbulent profile does not transition to the laminar profile over the length of the pipe included in the domain.

https://doi.org/10.1017/S0022112005003514 Published online by Cambridge University Press

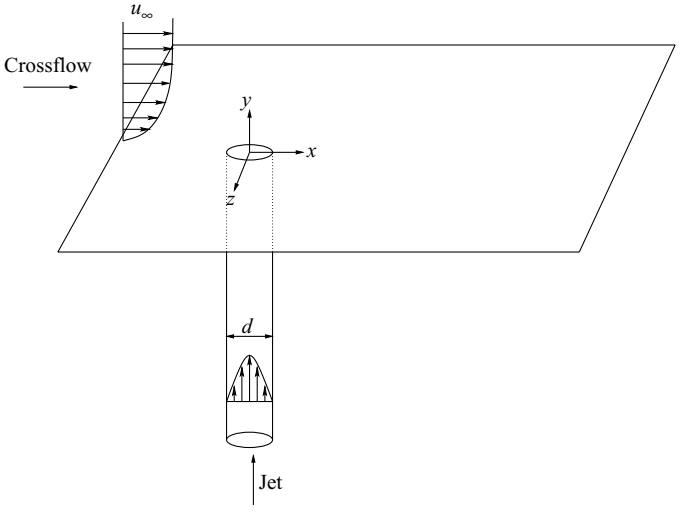


FIGURE 2. Schematic of the problem.

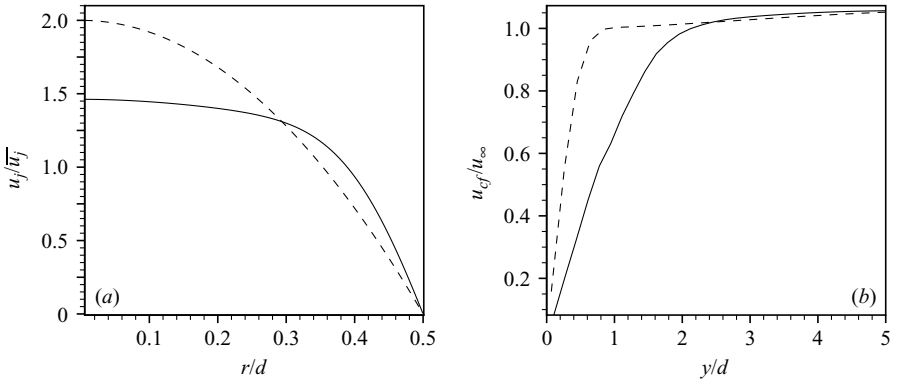


FIGURE 3. (*a*) Radial velocity variation of the two inflow profiles used for the jet: – – –, parabolic; ——, mean-turbulent profile. (*b*) Variation of the streamwise velocity with distance from the wall for two boundary layer profiles used for the crossflow: ——, $\delta_{80\%} = 1.32d$; – – –, $\delta_{80\%} = 0.44d$.

This behaviour will be clarified in § 3.3.1 which discusses the results. At the same velocity ratio, note that the jet with the parabolic velocity profile has a centreline velocity greater than the centreline velocity of the jet with the mean-turbulent profile. The difference in centreline velocities is about $0.5\overline{u}_j$. Two different boundary layer thicknesses are considered for the crossflow. At the location of the jet exit and in the absence of a jet, the first crossflow has an 80% boundary layer thickness of $1.32d$, and the second has a boundary layer that is three times thinner ($\delta_{80\%} = 0.44d$). Figure 3(*b*) shows the crossflow velocity variation with the distance from the wall for both the cases.

Table 1 describes the different simulations performed. The parameters include the velocity ratio r, jet velocity profile (either parabolic or mean-turbulent) and the crossflow boundary layer thickness. In addition to the eight possible combinations, a simulation at $r = 5.7$ using a parabolic profile and a crossflow with a very thick boundary layer ($\delta_{80\%} = 6.4d$ in the absence of the jet) was performed.

https://doi.org/10.1017/S0022112005003514 Published online by Cambridge University Press

Case	Velocity ratio r	Jet inlet profile	Crossflow boundary layer $\delta_{80\%}$
I	1.52	Parabolic	$1.32d$
II	1.52	Mean-turbulent	$1.32d$
III	1.52	Parabolic	$0.44d$
IV	1.52	Mean-turbulent	$0.44d$
V	5.7	Parabolic	$1.32d$
VI	5.7	Mean-turbulent	$1.32d$
VII	5.7	Parabolic	$0.44d$
VIII	5.7	Mean-turbulent	$0.44d$
IX	5.7	parabolic	$6.4d$

TABLE 1. Conditions for the various simulations performed.

2.2. *Numerical details*

The numerical scheme solves the incompressible Navier–Stokes equations

$$\frac{\partial u_i}{\partial t} + \frac{\partial u_i u_j}{\partial x_j} = -\frac{\partial p}{\partial x_i} + \nu \frac{\partial^2 u_i}{\partial x_j x_j}, \quad \frac{\partial u_i}{\partial x_i} = 0 \tag{2.1}$$

on unstructured grids. Here u_i, p and ν denote the velocities, pressure and kinematic viscosity respectively. The density of the fluid is assumed constant and is absorbed into the pressure. The numerical scheme has been described by Mahesh, Constantinescu & Moin (2004) and will not be dealt with here in detail. The algorithm stores the Cartesian velocities and the pressure at the centroids of the cells (control volumes) and the face normal velocities are stored independently at the centroids of the faces. The scheme is a predictor–corrector formulation which emphasizes discrete energy conservation on unstructured grids. This property makes the algorithm robust at high Reynolds numbers without numerical dissipation. The predicted velocities at the control volume centroids are obtained using the viscous and the nonlinear terms of equation (2.1) which are then used to predict the face normal velocities on the faces. The predicted face normal velocity is projected so that continuity is discretely satisfied. This yields a Poisson equation for pressure which is solved iteratively using a multigrid approach. The pressure field is used to update the Cartesian control volume velocities. Explicit time-advancing is performed using the Adams–Bashforth scheme and implicit time-stepping is performed using a Crank–Nicholson scheme. The algorithm has been validated for a variety of problems (see Mahesh *et al.* 2004) over a range of Reynolds numbers.

For the lower velocity ratio simulations, the computational domain spans $48d$ in the streamwise direction, $24d$ in the wall normal direction and $24d$ in the spanwise direction. The jet exit is at a distance $8d$ from the crossflow inflow plane. For the $r = 5.7$ simulations, the jet penetrates deeper, warranting a larger vertical extent. The computational domain in this case spans $48d \times 48d \times 48d$. The crossflow inflow plane is located $12d$ upstream of the jet exit for the $r = 5.7$ simulations. For all the simulations, the domain includes a $10d$ length of pipe upstream of the jet exit. This is to ensure that the jet develops naturally before issuing into the crossflow.

The computational mesh is unstructured and consists of hexahedral elements. The use of an unstructured mesh allows an efficient variation of the mesh size. Fine elements are used near the crossflow wall, pipe walls and near the jet exit. Relatively coarse elements are used far away from the jet exit in the free stream. The mesh

https://doi.org/10.1017/S0022112005003514 Published online by Cambridge University Press

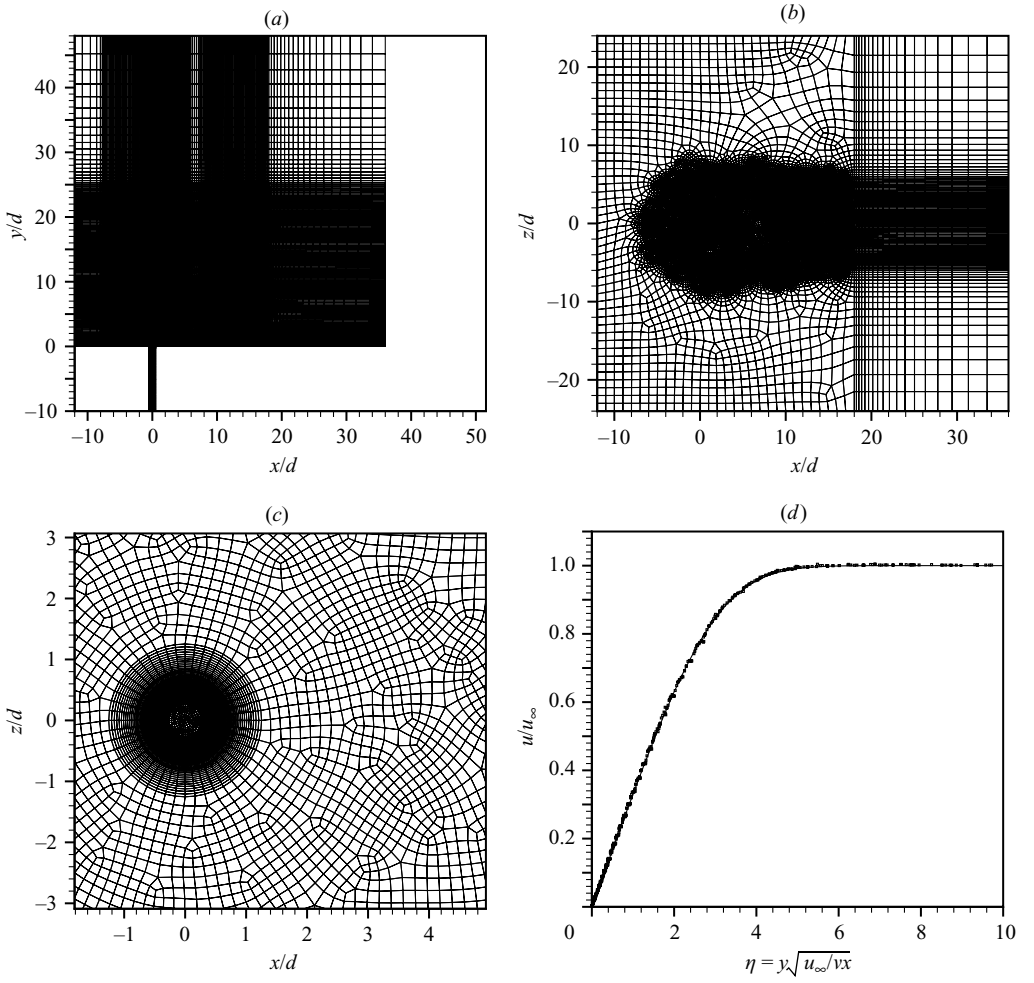


FIGURE 4. (*a*) The computational mesh on the symmetry plane for the simulations at $r = 5.7$. (*b*) Horizontal section of the mesh close to the wall. (*c*) Closer view of mesh around the jet exit. Note the unstructured elements and the rapid transition in mesh sizes. (*d*) Validation of the crossflow boundary layer. The solid line is the analytical Blasius solution for laminar flow past a flat plate; the symbols show the instantaneous velocity from the simulation.

size varies from $0.01d$ to $3d$ over the computational domain. Figure 4(*a*) shows a cross-section of the mesh on the symmetry plane and figure 4(*b*) shows a slice of the mesh parallel to the wall. Note the unstructured elements and the rapid variation in mesh size. A closer view is provided in figure 4(*c*) which shows the fine elements used near the jet exit. The mesh shown in these figures is the one used in the $r = 5.7$ simulations. The mesh is generated as follows. The mesh on the inflow plane of the pipe ($y/d = -10$) is generated first. A boundary layer is used to allow the mesh size to increase radially inward starting with $0.01d$ at the wall. The growth rate is 1.05. Once the radial element length reaches $0.1d$, the rest of the pipe cross-section is meshed using unstructured quadrilaterals of approximately the same edge length. The flat plate region ($y/d = 0$) is then meshed. The mesh size increases gradually radially outward from the pipe exit, starting from $0.01d$ at a growth rate of 1.05. This ensures

https://doi.org/10.1017/S0022112005003514 Published online by Cambridge University Press

a smooth variation in element size at the jet exit. The elements grow in this manner to an azimuthal size of $0.1d$ following which the element size is fixed to $0.1d$ over a region which roughly extends $12d$ in the span, $6d$ upstream and $20d$ downstream of the jet exit. The rest of the flat plate region away from the jet is then meshed, using larger quadrilateral elements as figure 4(*b*) shows. A volume grid is generated by sweeping the surface mesh on the pipe entrance and flat plate region in the vertical direction (y). The volume elements are therefore hexahedral prisms. The mesh size (Δy) at the wall is $0.01d$ and increases away from the wall at a growth rate of 1.05 till Δy is around $0.1d$ after which it is kept constant. Past $y = 24d$ (free stream), Δy grows more rapidly at a growth rate of 1.1 as observed in figure 4(*a*).

The boundary conditions are specified as follows. At the crossflow inflow plane, the velocities are specified as a function of y such that the boundary layer has the desired thickness at the location of the jet exit in the absence of the jet. The velocity field is specified according to the similarity solution for laminar flow past a flat plate (Schlichting 1968). The boundary layer is validated by performing a simulation with no jet and the solution is compared to the analytical Blasius boundary layer profile. Figure 4(*d*) shows this comparison. Instantaneous velocities (u) at all the elements in the computational domain are plotted against the similarity variable $\eta = y\sqrt{u_\infty/\nu x}$. Note the good agreement with the analytical solution. The mesh used for this comparison contained about a tenth of the elements used for the computations of a jet in crossflow. The other boundary conditions are as follows. At the inflow for the pipe, the velocity field is specified, based on r and the jet velocity profile, as a function of the radial distance. At the spanwise boundaries, the velocities are specified as for the crossflow inflow plane (as a function of x and y). At the top boundary, streamwise velocity of u_∞ is prescribed. A zero-gradient boundary condition is used at the outflow. Here and in the rest of the paper, the terminology used for velocities is u, v and w for velocities in the x-, y- and z-directions respectively.

The computations are initialized with just the crossflow. For the the $r = 1.52$ simulations, time advancement was explicit, while for the $r = 5.7$ simulations, time advancement was implicit. The computational time step is of the order of $0.001d/u_\infty$. The solution is advanced to about $60d/u_\infty$ to allow the initial transients to exit the domain before computing time-averaged statistics. Although the inflow is laminar, the solution is three-dimensional and unsteady. The unsteadiness is more pronounced at the higher velocity ratio. The time-averaged quantities presented in this paper are computed after the transients exit the domain.

3. Results

3.1. *Flow features*

This section presents some of the features observed in the results from the present simulations. Figure 5(*a*) shows instantaneous contours of the in-plane velocity ($\sqrt{u^2 + v^2}$) on the symmetry plane from results of simulation V where $r = 5.7$, the jet has a parabolic velocity profile at the inlet and $\delta_{80\%} = 1.32d$ for the crossflow. The unsteadiness of the flow is apparent, as are the small-scale features close to the jet exit. Figure 5(*b*) shows the contours of the time-averaged in-plane velocity ($\sqrt{u^2 + v^2}$) on the symmetry plane for an $r = 1.52$ jet in crossflow (simulation I: parabolic velocity profile for the jet; $\delta_{80\%} = 1.32d$). Note the low-velocity region just upstream of the jet exit. Also shown are a few characteristic streamlines on the symmetry plane. Note that upstream of the jet exit, crossflow fluid close to the wall appears to stagnate on encountering the jet. Streamlines downstream of the jet exit show entrainment of

https://doi.org/10.1017/S0022112005003514 Published online by Cambridge University Press

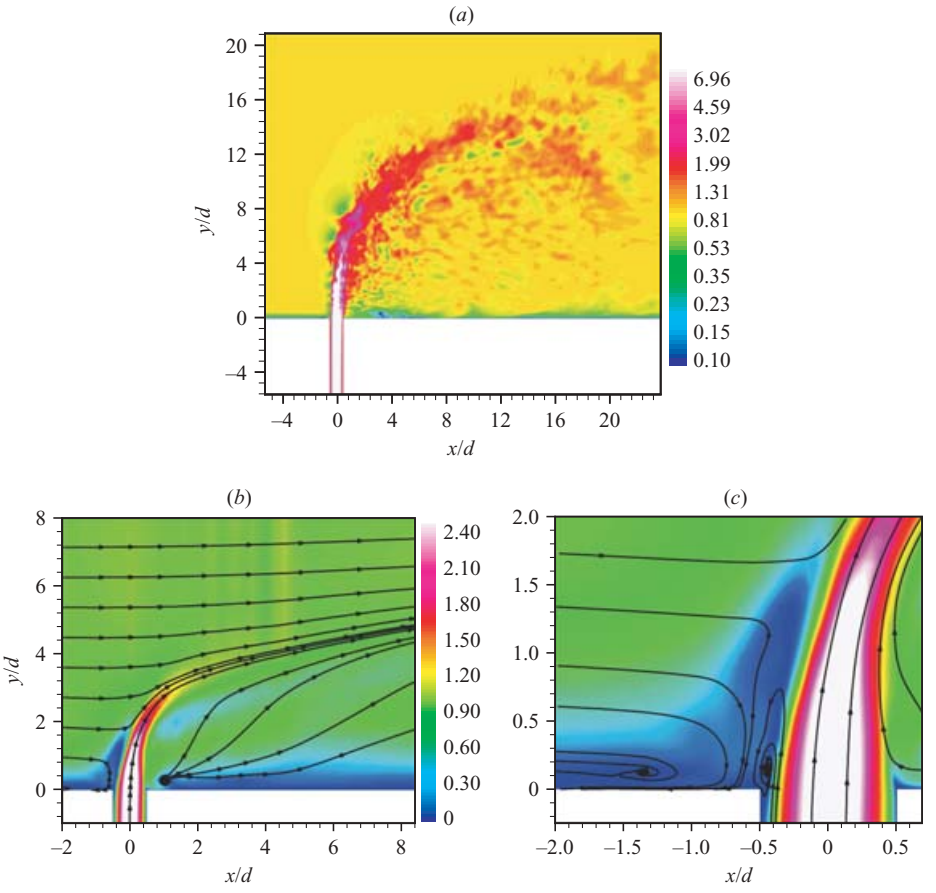


FIGURE 5. Contours of velocity on the symmetry plane. (*a*) Instantaneous contours of $\sqrt{u^2+v^2}$ ($r=5.7$; simulation V). (*b*) Time-averaged contours of $\sqrt{u^2+v^2}$ and some characteristic streamlines ($r=1.52$; simulation I). (*c*) Closer view of region near the jet exit. Note the horseshoe vortex upstream of the jet ($x/d=-1.4$) and the hovering vortex just above the jet exit. Parts (*b*) and (*c*) have the same colour scale.

the crossflow fluid. The existence of a node ($x/d\sim1.05$; $y/d\sim0.3$) with a positive divergence is seen. The presence of such a node above the wall and downstream of the jet exit has been noted by Kelso *et al.* (1996), Hasselbrink & Mungal (2001*b*) and others. A closer view of the region near the jet exit is presented in figure 5(*c*). The streamlines show the presence of a horseshoe vortex upstream of the jet exit ($x/d=-1.4$) and close to the wall. Just above the jet exit, near the leading edge, the streamline pattern shows another vortex. Kelso *et al.* (1996) term this a hovering vortex and their experiments showed it at $r=2.3$. The hovering vortex was observed in all the four simulations at the lower velocity ratio; it was not seen in any of the higher velocity ratio simulations.

3.2. *Jet trajectory*

Previous experimental studies have defined the jet trajectory using the local velocity maxima (Kamotani & Greber 1972) or the local scalar concentration maxima (Smith & Mungal 1998). This paper defines the trajectory as the streamline originating from the centre of the jet exit on the symmetry plane. Close to the jet exit, both

https://doi.org/10.1017/S0022112005003514 Published online by Cambridge University Press

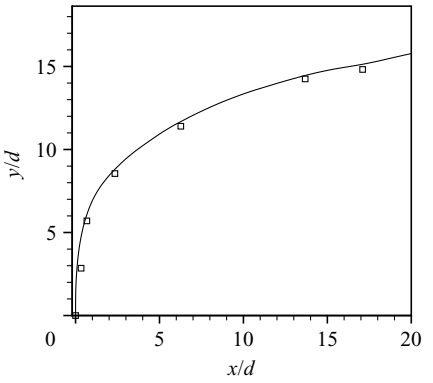


FIGURE 6. Comparison of jet trajectory to experiment: ——, simulation VI; □, Su & Mungal (2000).

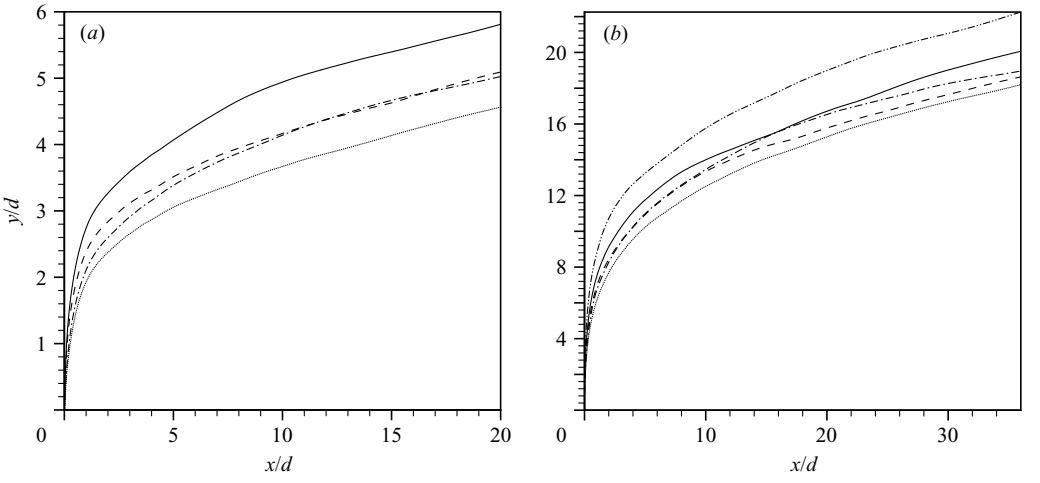


FIGURE 7. Comparison of the time-averaged jet trajectories. (*a*) $r = 1.52$: ——, I; – – – –, II; —·—, III; ·····, IV. (*b*) $r = 5.7$: ——, V; – – – –, VI; —·—, VII; ·····, VIII; —··—, IX. Note the significant difference in trajectories even between jets of the same r.

concentration and velocity have multiple maxima (Kamotani & Greber 1972; Yuan & Street 1998). This makes the definition of the trajectory using either of these techniques difficult. This issue is overcome defining the trajectory based on the streamline. Defining the trajectory based on the mean streamline also describes the path taken by the jet fluid more accurately. The trajectories presented in this section are computed using the time-averaged velocity field on the symmetry plane.

Figure 6 compares the jet trajectory extracted from simulation VI to that from the experiment of Su *et al.* (2000). Note that the trajectories show reasonable agreement. Both the simulation and the experiment have the same velocity ratio ($r = 5.7$) and the same crossflow boundary layer thickness ($\delta_{80\%} = 1.32d$). The jet in the simulation has a mean-turbulent velocity profile while the jet in the experiment is fully turbulent. We do not suggest that the interaction of a laminar jet with the crossflow is the same as that of a turbulent jet. However, it appears, at least for this case, that the trajectories are reasonably close. Figure 7 compares the jet trajectories obtained from the different

https://doi.org/10.1017/S0022112005003514 Published online by Cambridge University Press

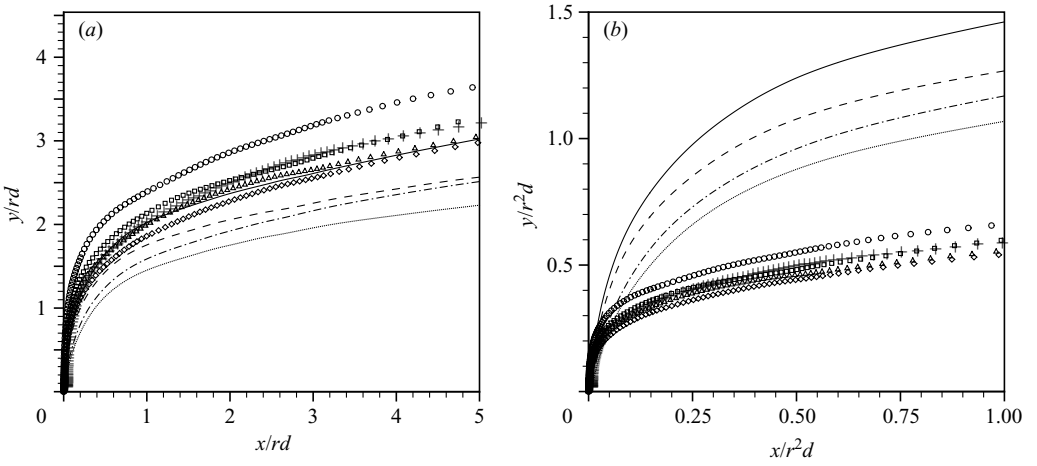


FIGURE 8. Comparison of the time-averaged jet trajectories – axes scaled by (*a*) rd and (*b*) r^2d: ——, I; – – – –, II; —·—, III; ·····, IV; □, V; △, VI; +, VII; ◇, VIII; ○, IX. Note the lack of collapse.

simulations. Trajectories from $r = 1.52$ simulations are presented in figure 7(*a*) and those from $r = 5.7$ simulations are presented in figure 7(*b*). The axes are non-dimensionalized by d. The trajectories show that the fluid in the pipe exits the jet, interacts with the crossflow fluid as it moves away from the jet exit and begins to bend in the direction of the crossflow. Close to the jet exit the trajectories are almost vertical. The jet with $r = 5.7$ penetrates deeper than the jet with $r = 1.52$ as expected. Significantly, trajectories of jets at the same r differ noticeably. This difference is attributable to variation of either the jet velocity profile or the crossflow boundary layer thickness.

Figure 8(*a*) evaluates the rd scaling using the trajectories from all the simulations. Figure 8(*b*) shows a similar comparison to evaluate the r^2d scaling. The absence of any kind of scaling collapse is apparent, though the rd scaling appears better than the r^2d scaling. The scatter seen in figure 8(*a*) shows that rd is not sufficient to scale trajectories, and that the jet velocity profile and the crossflow boundary layer thickness have to be taken into account to estimate the trajectory.

One possible approach to scale the trajectories is to compute the velocity ratio (r_{mod}) based on the integrated momentum flux of the jet and of the crossflow fluid, i.e.

$$r_{mod} = \left\{ \frac{\dfrac{1}{A}\displaystyle\int_A \rho_j u_j^2 \, \mathrm{d}A}{\dfrac{1}{\delta}\displaystyle\int_0^{\delta} \rho_{cf} u_{cf}^2 \, \mathrm{d}y} \right\}^{1/2}, \tag{3.1}$$

where A is the cross-section area of the jet. Here, r_{mod}^2 denotes the ratio of the momentum of the jet fluid to that of the crossflow fluid. Note that r_{mod} is sensitive to both the jet velocity profile and the crossflow velocity profile. Figure 9(*a*) shows the trajectories from all the simulations scaled with $r_{mod}d$. Hasselbrink & Mungal (2001*a*) suggest that expressing the numerator in equation (1.1) in terms of the averaged momentum flux per unit area of the jet might help scale the trajectories. Such a

https://doi.org/10.1017/S0022112005003514 Published online by Cambridge University Press

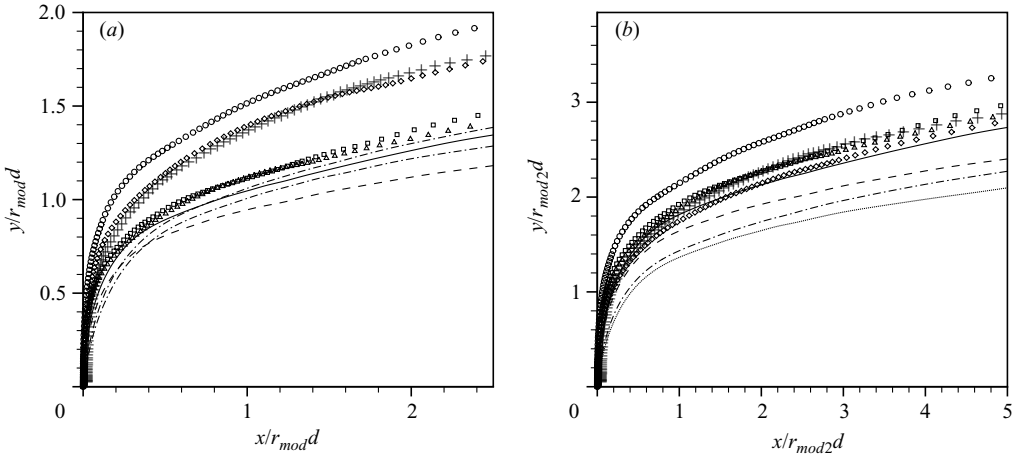


FIGURE 9. Comparison of the time-averaged jet trajectories – axes scaled by r_{mod} and r_{mod2} which are defined in equations (3.1) and (3.2) respectively: ——, I; – – – –, II; —·—, III; ·····, IV; □, V; △, VI; +, VII; ◇, VIII; ○, IX. Note the lack of collapse.

modified velocity ratio r_{mod2} can be expressed as

$$r_{mod2} = \left\{ \frac{\dfrac{1}{A}\displaystyle\int_A \rho_j u_j^2 \, \mathrm{d}A}{\rho_{cf} u_{cf}^2} \right\}^{1/2} . \tag{3.2}$$

This modified velocity ratio is clearly dependent on the jet velocity profile. Figure 9(*b*) shows the trajectories from the simulations scaled using $r_{mod2}d$. Note that the trajectories scaled using both r_{mod} and r_{mod2} show scatter comparable to that seen in figure 8(*a*), indicating that such approaches are not adequate to scale the trajectories.

3.2.1. *Effect of jet velocity profile*

The effect of the jet velocity profile on the trajectory can be seen by comparing trajectories of cases I and II (figure 7*a*). Both the jets have a velocity ratio 1.52 and a crossflow boundary layer thickness $\delta_{80\%} = 1.32d$. They only differ in the jet velocity profile and hence the peak (centreline) velocity. The trajectories show that the jet with the parabolic profile (simulation I) and a higher centreline velocity penetrates deeper than the jet with the mean-turbulent profile (simulation II). It can be seen that close to the jet exit both the trajectories are identical and that the mean-turbulent jet deflects and bends into the crossflow before the parabolic jet does. Similar comparison of trajectories from other simulations (III *vs.* IV, V *vs.* VI and VII *vs.* VIII) show the same behaviour. The jet with the parabolic velocity profile penetrates deeper than the jet with the mean-turbulent profile when r and $\delta_{80\%}$ are the same.

3.2.2. *Effect of crossflow boundary layer*

Comparison of trajectories from simulations I and III demonstrates the effect of the crossflow boundary layer thickness on jet trajectory. Both the simulations are at $r = 1.52$ and the jet velocity profile is parabolic at the pipe inflow. They issue, however, into crossflows with different boundary layer thickness. When the boundary layer is thicker (I), the jet penetrates deeper into the crossflow than when the boundary layer is thinner (III). This behaviour may be explained by the fact that the thinner

https://doi.org/10.1017/S0022112005003514 Published online by Cambridge University Press

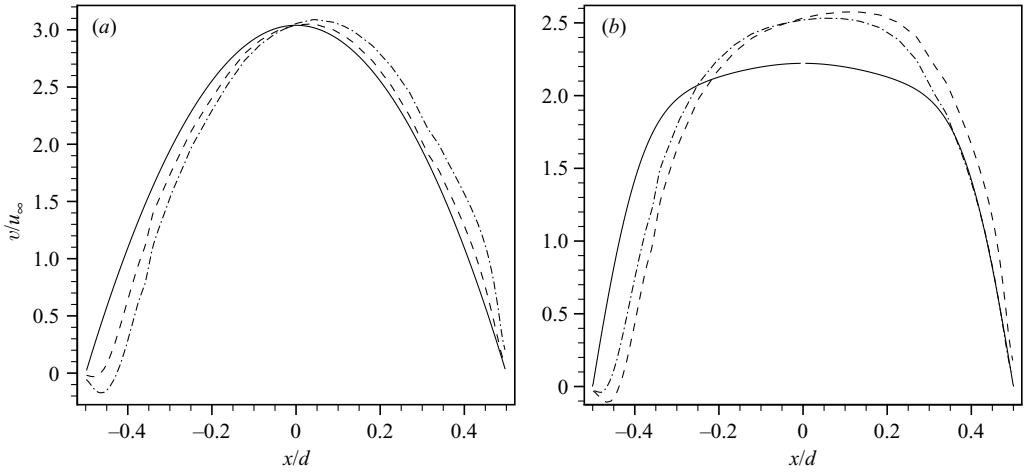


FIGURE 10. Comparison of the time-averaged velocity (v) at the jet exit for $r = 1.52$: (a) ——, pipe inflow; – – – –, I; —·—, III; (b) ——, pipe inflow; – – – –, II; —·—, IV.

boundary layer has more momentum close to the jet exit, as a result of which the jet bends earlier compared to a similar jet entering a crossflow with a thicker boundary layer. A similar trend was observed in Su & Mungal's (2000) experiments where the jet penetrates further into the flow when the nozzle is flush with the floor, compared to when the nozzle protrudes into the flow. Again, comparison of trajectories from other pairs of simulations (II *vs.* IV, V *vs.* VII and VI *vs.* VIII) where only the crossflow boundary layer thickness differs shows the same trend. The jet penetrates further when δ is larger. Note that the trajectories from simulations V and IX ($r = 5.7$; parabolic profile for the jet) show a larger difference since the crossflow boundary layer thickness varies by a factor of 5.

3.3. *Near field*

The above effects of the jet velocity profile and crossflow boundary layer thickness on the jet trajectory are explained below. Both parameters significantly influence the near field of the jet exit which in turn affects the trajectory.

3.3.1. *Description of the near field*

The velocity profile at the jet exit is not the same as that at the inflow of the pipe. Representative exit velocity profiles are shown in figures 10 and 11. The solid line in these plots shows the velocity profile at the inflow of the pipe. Figure 10(a) compares the exit profiles of simulations I and III, where $r = 1.52$ and the jets have a parabolic profile at the inflow. The jet accelerates between the pipe inflow and the jet exit as can be seen from the increase in the peak velocity. Also, the location of the peak moves from the centreline (at the pipe inflow) to the right (at the jet exit). The crossflow in simulation III has a lower δ than the crossflow in simulation I, and it can be seen that the thinner crossflow boundary layer enhances the shift in the profile – both in the the value of v_{max} and in the x/d location of v_{max}. Figure 10(b) makes a similar comparison for jets with a mean-turbulent velocity profile (simulations II and IV; $r = 1.52$). The jet in II issues into a crossflow that has a thicker boundary layer than in IV. The increase in v_{max} in these cases is higher than is observed for I and III and the rightward shift of the velocity maximum location is also more pronounced. The thinner boundary layer again enhances the shift in the velocity profile. All the

https://doi.org/10.1017/S0022112005003514 Published online by Cambridge University Press

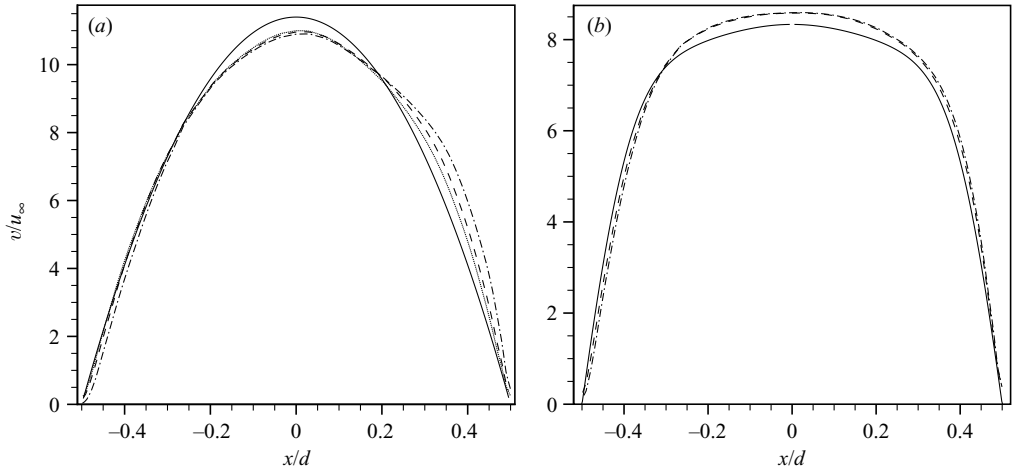


FIGURE 11. Comparison of the time-averaged velocity (v) at the jet exit for $r = 5.7$: (a) ——, pipe inflow; – – – –, V; —·—, VII; ·····, IX; (b) ——, pipe inflow; – – – –, VI; —·—, VIII.

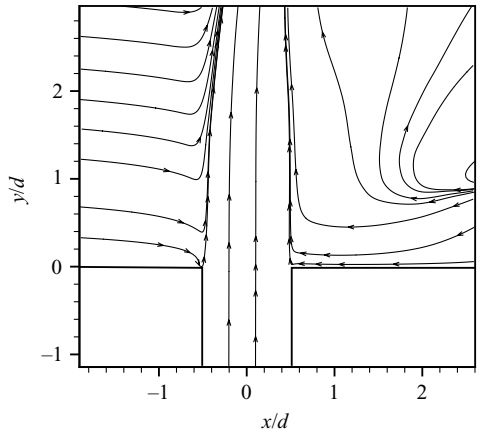


FIGURE 12. Streamlines shown on the symmetry plane for a simulation with $r = 5.7$. Despite the absence of reverse flow into the pipe, note the tendency of some crossflow fluid to move 'towards' the jet exit.

plots show that close to the leading edge of the jet ($x/d \sim -0.5$), there is a region of negative velocity and hence a region where the crossflow fluid enters the jet. Note that higher reverse flow velocities are seen when the crossflow boundary layer is thinner (simulations II and IV).

Velocity profiles at the jet exit for the $r = 5.7$ simulations (simulations V to IX) are presented in figure 11. Similar trends are seen – rightward shift of the profile and an acceleration of the fluid near the trailing edge. None of the plots show a reverse flow at the jet exit (in contrast to figures 10a and 10b). However, the streamlines show a negative v velocity upstream of the jet exit and the crossflow fluid flowing towards the jet exit (see figure 12). The higher momentum of the jet fluid prevents any of the crossflow fluid entering the pipe and hence no reverse flow is seen at the jet exit.

This reverse flow is a result of a separation of the jet fluid inside the pipe and is shown more clearly in figure 13. Shown are the streamlines on the wall of the pipe

https://doi.org/10.1017/S0022112005003514 Published online by Cambridge University Press

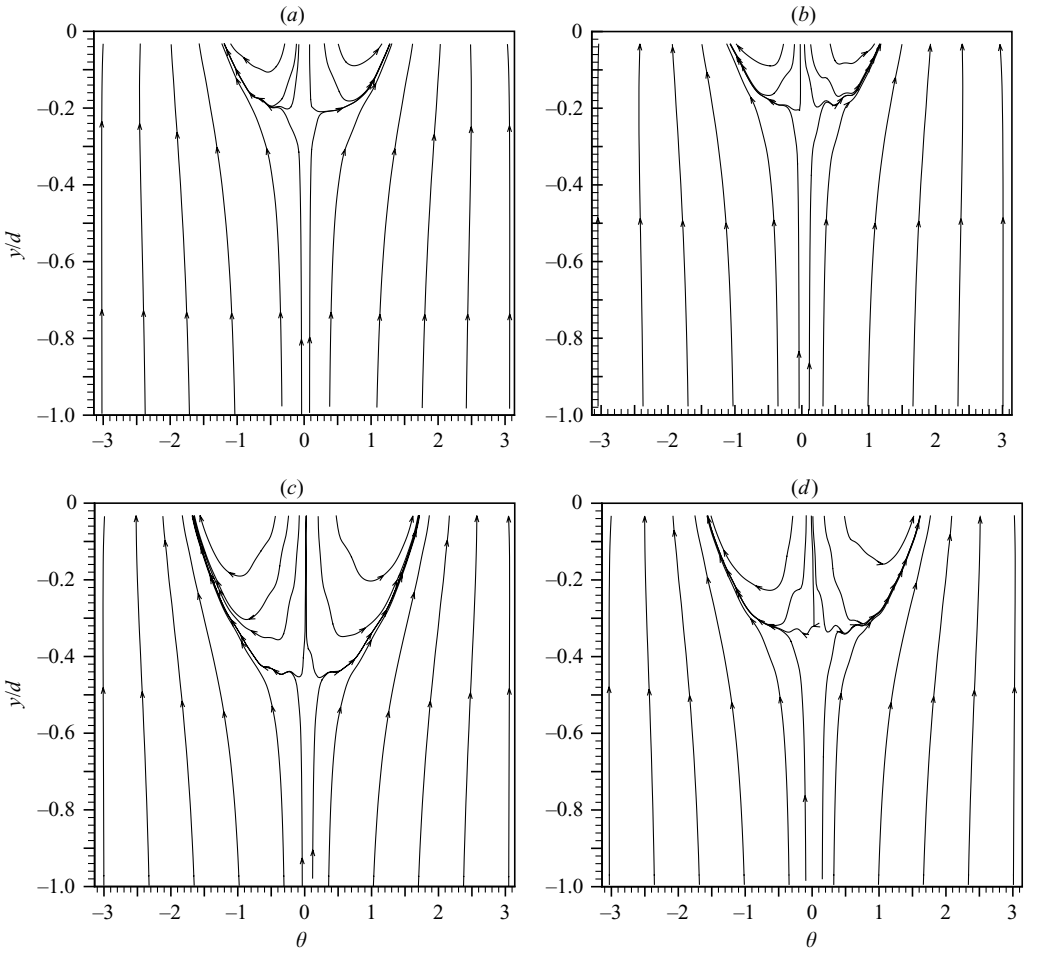


FIGURE 13. Streamlines on the pipe wall shown for simulations I, II, III and IV, (*a*)–(*d*) respectively. $\theta = 0$ is the leading edge of the pipe around which the crossflow fluid enters the pipe.

from simulations I, II, III and IV. The plots should be interpreted as though the pipe was slit along its length at the trailing edge ($x/d = 0.5$) and spread out. Such a visualization of the surface streamline pattern in the pipe has been suggested by Kelso *et al.* (1996). These streamlines are generated using the two-dimensional velocity field in cylindrical coordinates (u_θ and u_y; $u_r = 0$) on the wall of the pipe. $y/d = 0$ is the jet exit, $\theta = 0$ indicates the leading edge and $\theta = -\pi$ and $\theta = \pi$ join to form the trailing edge of the pipe. Crossflow fluid enters the pipe at and near the leading edge and exits the jet exit plane on the sides of the pipe ($\theta \sim \pm(1.25\text{–}1.5)$). The streamline pattern is symmetric about $\theta = 0$ as is expected. This downward flow of the crossflow fluid (opposing the 'upward' flow of the jet fluid) sets up a separation point which is clearly seen from these plots. The location of this point suggests the extent to which crossflow fluid enters the pipe. It is seen that a change in velocity profile does not change the streamline pattern, as seen by comparing I with II, and III with IV. The fluid has very low velocity close to the wall (irrespective of the profile) and this makes the jet velocity profile unimportant. The reverse flow does show a dependence on the crossflow boundary layer, which is observed by comparing I with III, and II with IV.

https://doi.org/10.1017/S0022112005003514 Published online by Cambridge University Press

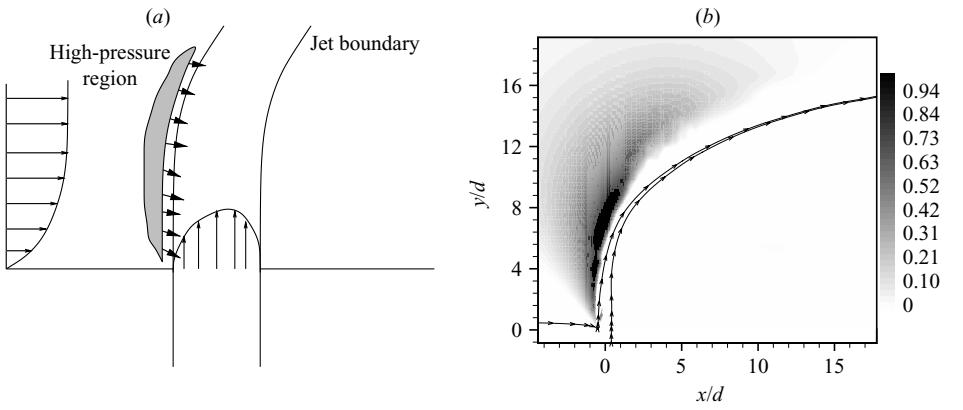


FIGURE 14. (*a*) Schematic of the near field. (*b*) Contours of the pressure coefficient C_p from simulation VI. Notice the high-pressure region upstream of the jet.

Greater reverse flow and a lower separation point are noticed when the boundary layer gets thinner (simulations II and IV).

This behaviour shows the need to allow for a finite length of pipe in simulations of jets in crossflow. A similar conclusion was reached by Yuan *et al.* (1999) in their simulations at velocity ratios 2–4. Yuan *et al.* show that simulations without a finite pipe length give unphysical results. This behaviour is explained by figures 10 and 11 which show that the flow at the jet exit is different from that at the pipe inflow. Section 3.3.2 explains this trend as a result of the interaction between the crossflow and the flow in the pipe. When the pipe is absent there is no reverse flow into the pipe and the resulting asymmetry in the velocity profile at the jet exit. Simulating flow inside the pipe seems increasingly important at lower velocity ratios. A conservative estimate of the required pipe length is $1d$. Note that these conclusions are drawn from the present simulations where the pipe length was $10d$. Also note that the Reynolds numbers in the present simulations are high enough that the mean-turbulent profile does not transition to the laminar profile over $10d$ length of the pipe as figures 10(*b*) and 11(*b*) show. The observed differences between the inflow profile and the jet-exit profile are due to the interaction of the jet with the crossflow.

3.3.2. *Explaining the near field*

In the absence of a crossflow, the jet behaves as a simple jet, the fluid decelerating as it moves away from the jet exit. In the absence of a jet, the crossflow would behave as a laminar flow over a flat plate. When both are present, the jet is seen as an obstacle in the path of the crossflow. This is particularly true close to the wall. The near field and the trajectory of the jet can be explained as a result of the competing inertias of the jet and the crossflow.

Figure 14(*a*) is a schematic of the near field of the jet exit. The symmetry plane is shown. The jet is represented by a jet boundary extending from the jet exit. On the symmetry plane, the boundary can be represented by two streamlines, one beginning at the leading edge of the jet exit and the other beginning at the trailing edge (these streamlines and the jet boundary can be seen clearly in figure 12). Also shown is a velocity (u) profile for the crossflow to indicate a y dependence and a velocity (v) profile for the jet which is a function of x and z on the jet exit plane.

Close to the jet exit, the velocity and momentum of the crossflow are perpendicular to those of the jet. The jet acts like an obstacle in the path of the crossflow fluid and

https://doi.org/10.1017/S0022112005003514 Published online by Cambridge University Press

a region of high pressure is set up upstream of the jet as shown. Sample contours of the pressure coefficient ($C_p = (p - p_\infty)/u_\infty^2$) on the symmetry plane are shown in figure 14(*b*), where p_∞ is the free-stream pressure at the crossflow inlet. Note the high pressure upstream of the jet beginning close to jet exit. Velocity contours in figure 5(*b*) show that this region is characterized by low velocities. Streamlines on the (x, z)-plane (parallel to the wall) close to the wall show crossflow fluid from upstream of the jet exit going around the jet, similar to flow around obstacles. The high-pressure region sets up an adverse pressure gradient in the vertical direction which pushes crossflow fluid towards the jet exit as seen in the downward curvature of streamlines upstream and close to the jet exit (figures 5*b* and 12). When the jet has a lower momentum, as in the $r = 1.52$ case, the adverse pressure gradient succeeds in forcing crossflow fluid into the pipe (figures 10*a* and 10*b*). To conserve mass, the jet fluid towards the trailing edge accelerates which results in the rightward shift of velocity profiles as observed.

When the crossflow boundary layer is thinner, the momentum of the crossflow fluid closer to the jet exit increases. As a result, the high-pressure region moves closer to the jet exit. This causes the velocity profile shift at the jet exit to be greater in cases with thinner crossflow boundary layer as was observed (figures 10 and 11). A thinner boundary layer also causes a greater adverse pressure gradient into the pipe which in turn drives more crossflow fluid into the pipe. This behaviour is noticed as increased negative velocities at the leading edge of the jet exit (figure 10), more reverse flow (figure 13) and an earlier separation point in the pipe.

4. A simple scaling law for the trajectory

The deflection of the jet is a result of the inertial momentum of the crossflow opposing and, eventually, overcoming the momentum of the jet. Close to the jet exit, the jet has a higher overall momentum than that of the crossflow which is at a low velocity. This causes the trajectory to be almost vertical as seen earlier. Moving away from the jet exit, the velocity of the crossflow fluid increases (until it reaches u_∞ whereafter it is constant) and velocity of jet fluid decreases. Figure 7(*a*) shows that the jets with $r = 1.52$ undergo a rapid deflection past $y/d \sim 1.5$. The jets with $r = 5.7$ (figure 7*b*) all show a similar deflection past $y/d \sim 6$.

A simple model for the trajectory is proposed. The model is restricted to jets with a circular cross-section. Note that in the near field, the jet remains vertical up to a point beyond which it rapidly deflects into the crossflow. Let h denote the height up to which the jet is vertical. In the near field, the jet may be approximated by a cylinder of diameter d and a height h, which interacts with the crossflow. It is postulated that the jet deflects due to the competing effects of the pressure gradient imposed by the crossflow (figure 14*b*) and the inertia of the jet in the vertical direction. The pressure gradient imposed by the crossflow scales with the crossflow momentum flux,

$$\rho_{cf} d \int_0^h u_{cf}^2 \, \mathrm{d}y. \tag{4.1}$$

Note that u_{cf} varies with y and hence depends on the crossflow boundary layer thickness. The vertical momentum flux of the jet is represented by

$$\rho_j \int_A u_j^2 \, \mathrm{d}A. \tag{4.2}$$

https://doi.org/10.1017/S0022112005003514 Published online by Cambridge University Press

Simulation	r	Velocity profile	d_j/d	$\delta_{80\%}$	h/d
I	1.52	parabolic	1.15	1.32d	0.61
II	1.52	mean-turb	1.09	1.32d	0.53
III	1.52	parabolic	1.15	0.44d	0.32
IV	1.52	mean-turb	1.09	0.44d	0.26
V	5.7	parabolic	1.15	1.32d	2.57
VI	5.7	mean-turb	1.09	1.32d	2.38
VII	5.7	parabolic	1.15	0.44d	1.85
VIII	5.7	mean-turb	1.09	0.44d	1.76
IX	5.7	parabolic	1.15	6.4d	3.14

TABLE 2. Values of near-field scaling parameter h computed from the trajectories.

Note that u_j depends on the jet velocity profile. It is assumed that the jet begins to deflect when the cumulative effect of the pressure gradient on the jet becomes comparable to the vertical momentum flux, i.e.

$$\rho_{cf} d \int_0^h u_{cf}^2 \, \mathrm{d}y = C_m \rho_j \int_A u_j^2 \, \mathrm{d}A, \tag{4.3}$$

where C_m is a proportionality constant. The velocity profile of the jet may be parameterized in terms of an effective diameter d_j which is defined such that

$$\rho_j \int_A u_j^2 \, \mathrm{d}A = \frac{\pi d_j^2}{4} \rho_j \overline{u_j}^2 \tag{4.4}$$

where $\overline{u_j}$ denotes the mean velocity of the jet. Note that d_j equals d for a jet with a top-hat profile. For the two jet velocity profiles considered in this paper, d_j/d is higher for the jet with a parabolic profile than for the jet with a mean-turbulent profile (see table 2). Defining d_j allows a comparison between jets of the same rd but different velocity profiles. Equation (4.3) may be rewritten in terms of r as

$$\int_0^h d \left\{ \frac{u_{cf}}{u_\infty} \right\}^2 \mathrm{d}y = C_m r^2 \pi \frac{d_j^2}{4}. \tag{4.5}$$

Equation (4.5) explains the behaviour seen in the simulations. When the velocity ratio r increases, h increases to satisfy equation (4.5) and hence the jet deflects later. Recall that at the same velocity ratio and crossflow boundary layer thickness, a jet with parabolic velocity profile penetrates deeper into the crossflow than a jet with mean-turbulent velocity profile. The parabolic profile jet has a higher d_j/d and a higher momentum flux (right-hand side of equation (4.5)) and hence h needs to be higher compared to the mean-turbulent profile jet. This causes the parabolic jet to deflect later and penetrate deeper into the crossflow. Also recall that between two jets with the same velocity profile and velocity ratio, when the crossflow boundary layer is thinner, the jet penetrates less. For the same jet momentum flux, h needs to be smaller when the boundary layer is thinner (lower δ) in order to satisfy equation (4.5). This causes the jet in a thinner crossflow to deflect earlier, penetrating less. Equation (4.5) may be written as

$$\int_0^\delta d \left\{ \frac{u_{cf}}{u_\infty} \right\}^2 \mathrm{d}y + \int_\delta^h d \left\{ \frac{u_{cf}}{u_\infty} \right\}^2 \mathrm{d}y = C_m r^2 \pi \frac{d_j^2}{4}, \tag{4.6}$$

https://doi.org/10.1017/S0022112005003514 Published online by Cambridge University Press

where the crossflow momentum flux term has been split into two components. The first term is the momentum flux due to the crossflow fluid in the boundary layer and the second term is the momentum flux due to the crossflow fluid outside the boundary layer. Since h increases with r, the ratio of the first term to the second term in equation (4.6) decreases with increasing r. Hence, the contribution of the first term to the left-hand side of equation (4.5) gets smaller at higher r. This reduces the dependence of h (and hence the jet trajectory) on δ at higher velocity ratios.

In practice, h may be extracted from a trajectory as the y-coordinate at a small distance x downstream of the jet exit. Table 2 shows h extracted in this manner from the different simulations. Here, h is the y-coordinate of the trajectory at $x = 0.05d$. Note that the above mentioned dependence of h on the jet velocity profile and the crossflow boundary layer thickness is observed in table 2. A similar dependence is seen when h is defined as the y-coordinate of the trajectory at $x = 0.1d$. The fact that h depends on both the jet profile and the crossflow profile suggests that h be used to scale the trajectories. When the trajectories from the simulations are expressed in terms of the power law fit

$$\frac{y}{rd} = A\left(\frac{x}{rd}\right)^{B}, \tag{4.7}$$

the value of A ranges between 1.45 and 2.39. The value of B shows a relatively smaller range, $0.32 < B < 0.34$. A correlation of h and A shows $A \propto (h/d)^{0.15}$. Including h into the trajectory scaling yields

$$\frac{y}{rd} = A'\left(\frac{x}{rd}\right)^{B}\left(\frac{h}{d}\right)^{C}, \tag{4.8}$$

where A' is a constant, and $C = 0.15$. An analytical approach to estimate h is provided below. The crossflow velocity u_{cf} may be approximated as a piecewise linear function of y as

$$u_{cf} = \frac{u_\infty}{\delta} y \quad \text{when} \quad y \leqslant \delta, \quad u_{cf} = u_\infty \quad \text{when} \quad y \geqslant \delta. \tag{4.9}$$

Expressing u_{cf} in this manner, equation (4.5) may be written as

$$\left.\begin{aligned} d\int_0^h \left\{\frac{y}{\delta}\right\}^2 \mathrm{d}y = C_m r^2 \pi \frac{d_j^2}{4}, \ \text{when } h \leqslant \delta, \\ d\int_0^\delta \left\{\frac{y}{\delta}\right\}^2 \mathrm{d}y + d\int_\delta^h \mathrm{d}y = C_m r^2 \pi \frac{d_j^2}{4}, \ \text{when } h \geqslant \delta \end{aligned}\right\} \tag{4.10}$$

which, upon evaluating the integrals, becomes

$$\left.\begin{aligned} \frac{d}{\delta^2}\frac{h^3}{3} = C_m r^2 \pi \frac{d_j^2}{4}, \ \text{when } h \leqslant \delta, \\ d\left(h - \tfrac{2}{3}\delta\right) = C_m r^2 \pi \frac{d_j^2}{4}, \ \text{when } h \geqslant \delta. \end{aligned}\right\} \tag{4.11}$$

Finally, h may be written as

$$\left.\begin{aligned} \frac{h}{d} = \left\{\frac{3}{4}\pi C_m r^2 \frac{\delta^2 d_j^2}{d^4}\right\}^{1/3}, \ \text{when } h \leqslant \delta, \\ \frac{h}{d} = \frac{2}{3}\frac{\delta}{d} + \frac{\pi}{4} C_m r^2 \frac{d_j^2}{d^2}, \ \text{when } h \geqslant \delta. \end{aligned}\right\} \tag{4.12}$$

https://doi.org/10.1017/S0022112005003514 Published online by Cambridge University Press

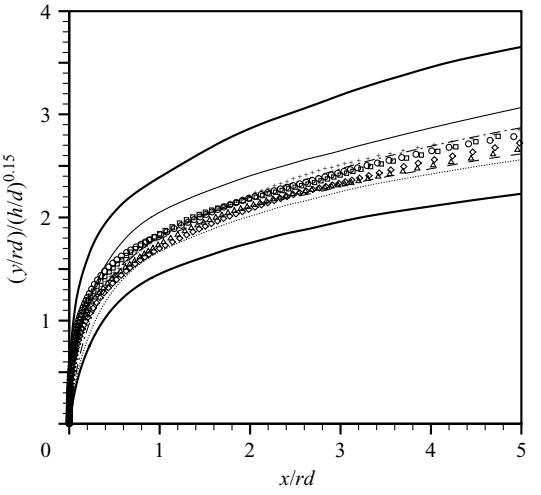


FIGURE 15. Trajectories scaled using h. Thick lines show the scatter bounds using rd scaling. h is computed using a piecewise linear function for u_{cf} in equation (4.5). Trajectories shown are from all the simulations: ——, I; – – – –, II; —·—, III; ·····, IV; □, V; △, VI; +, VII; ◇, VIII; ○, IX.

The unknown in equation (4.12) is C_m. Note the form of equation (4.12). h is less than δ only at low velocity ratios, and for most cases, $h \geqslant \delta$ applies. Equation (4.12) shows that as r increases, h increases. At high velocity ratios, the contribution of the $\frac{2}{3}\delta d$ term to h decreases indicating that the crossflow boundary layer thickness has a weak influence on h and the trajectory. These trends are in agreement with observed results. Substituting the values from table 2 (where h is extracted from the trajectory) gives $C_m \sim 0.05$. The values of h computed using equation (4.12) and $C_m = 0.05$ are used to scale the trajectories in figure 15. Solid thick lines are used to represent the scatter in the rd scaling corresponding to the rd scaled trajectories of the jet that penetrates the furthest (simulation IX) and the one that penetrates the least (simulation IV) into the crossflow. Note the reduction in scatter. The improved scaling supports the use of h to represent the effect of the jet velocity profile and the crossflow boundary layer on the jet trajectory.

5. Summary

Trajectories of a jet in crossflow are at present scaled by rd. However, the scaled trajectories from different experiments show a considerable scatter. Round jets in crossflow are studied using direct numerical simulation on an unstructured mesh. The simulations are performed at two velocity ratios – 1.5 and 5.7. By varying the crossflow boundary layer thickness and the jet velocity profile, it is shown that the trajectory depends on both these parameters. A jet with a higher centreline velocity issuing into a crossflow with a thicker boundary layer penetrates deeper compared to other jets at the same jet-to-crossflow velocity ratio. The jet trajectory is shown to be determined by the near field of the jet exit. A length scale h is proposed that parameterizes the relative inertia of the jet and the crossflow. This length scale takes into account both the jet velocity profile and the crossflow boundary layer thickness. An analytical expression for h is derived. Trajectories are scaled using h and the scaled trajectories show a significantly better collapse.

https://doi.org/10.1017/S0022112005003514 Published online by Cambridge University Press

This work was supported by the National Science Foundation under grant CTS-0133837. Computer time was provided by the Minnesota Supercomputing Institute and the San Diego Supercomputer Center.

REFERENCES

Andreopoulos, J. & Rodi, W. 1984 Experimental investigation of jets in a crossflow. *J. Fluid Mech.* **138**, 93–127.

Broadwell, J. E. & Breidenthal, R. E. 1984 Structure and mixing of a transverse jet in incompressible flow. *J. Fluid Mech.* **148**, 405–412.

Chochua, G., Shyy, W., Thakur, S., Brankovic, A., Lienau, K., Porter, L. & Lischinsky, D. 2000 A computational and experimental investigation of turbulent jet and crossflow interaction. *Numer. Heat Transfer* A **38**, 557–572.

Fearn, R. L. & Weston, R. P. 1974 Vorticity associated with a jet in crossflow. *AIAA J.* **12**, 1666–1671.

Fric, T. F. & Roshko, A. 1994 Vortical structure in the wake of a transverse jet. *J. Fluid Mech.* **279**, 1–47.

Hasselbrink, E. F. & Mungal, M. G. 2001*a* Transverse jets and jet flames. Part 1. Scaling laws for strong transverse jets. *J. Fluid Mech.* **443**, 1–25.

Hasselbrink, E. F. & Mungal, M. G. 2001*b* Transverse jets and jet flames. Part 2. Velocity and OH field imaging. *J. Fluid Mech.* **443**, 27–68.

Kamotani, Y. & Greber, I. 1972 Experiments on turbulent jet in a crossflow. *AIAA J.* **10**, 1425–1429.

Karagozian, A. R. 1986 An analytical model for the vorticity associated with a transverse jet. *AIAA J.* **24**, 429–436.

Keffer, J. F. & Baines, W. D. 1963 The round turbulent jet in a cross wind. *J. Fluid Mech.* **15**, 481–496.

Kelso, R. M., Lim, T. T. & Perry, A. E. 1996 An experimental study of round jets in cross-flow. *J. Fluid Mech.* **306**, 111–144.

Kelso, R. M. & Smits, A. J. 1995 Horseshoe vortex systems resulting from the interaction between a laminar boundary layer and a transverse jet. *Phys. Fluids* **7**, 153–158.

Krothapalli, A., Lourenco, L. & Buchlin, J. M. 1990 Separated flow upstream of a jet in a crossflow. *AIAA J.* **28**, 414–420.

Mahesh, K., Constantinescu, G. & Moin, P. 2004 A numerical method for large-eddy simulation in complex geometries. *J. Comput. Phys.* **197**, 215–240.

Margason, R. J. 1993 Fifty years of jet in crossflow research. In *AGARD Symp. on a Jet in Cross Flow, Winchester, UK, AGARD CP*-534.

Pratte, B. D. & Baines, W. D. 1967 Profiles of the round turbulent jet in a cross flow. *J. Hydraul. Div., ASCE* **92** (HY6), 53–64.

Schlichting, H. T. 1968 *Boundary Layer Theory*. McGraw Hill.

Schluter, J. U. & Schonfeld, T. 2000 LES of Jets in crossflow and its application to a gas turbine burner. *Flow Turbulence Combust.* **65**, 177–203.

Shan, J. W. & Dimotakis, P. E. 2001 Turbulent mixing in transverse jets. *GALCIT FM*: 2001.006.

Smith, S. H. & Mungal, M. G. 1998 Mixing, structure and scaling of the jet in crossflow. *J. Fluid Mech.* **357**, 83–122.

Su, L. K., Han, D., Miraflor, M. & Mungal, M. G. 2000 Measurements of scalar and velocity fields in turbulent crossflowing jets with low velocity ratio. *AIAA Paper* 2000-815, pp. 1–11.

Yuan, L. L. & Street, R. L. 1998 Trajectory and entrainment of a round jet in crossflow. *Phys. Fluids* **10**, 2323–2335.

Yuan, L. L., Street, R. L. & Ferziger, J. H. 1999 Large-eddy simulations of a round jet in crossflow. *J. Fluid Mech.* **379**, 71–104.

https://doi.org/10.1017/S0022112005003514 Published online by Cambridge University Press